Green Chemistry

ROYAL SOCIETY OF CHEMISTRY

PAPER

View Article Online
View Journal | View Issue

Cite this: *Green Chem.*, 2024, **26**, 6501

Facile preparation of lignocellulosic xerogels by alkali freezing and ambient drying†

Qiaoling Huang,‡[a] Zerong Li,‡[a] Jialong Hu,[a] Wei Wang[a,b] and Wei Li *[a]

Received 17th February 2024,
Accepted 15th April 2024

DOI: 10.1039/d4gc00825a

rsc.li/greenchem

Recently, the ambient drying method for the preparation of xerogels has attracted great attention due to its low cost and high drying efficiency. However, the strong capillary forces existing during ambient drying cause severe shrinkage or even collapse of the aerogels (called xerogels). Although chemical cross-linking or displacement of water by organic solvents have been tried to solve the problem, extensive usage of chemicals and time-consuming displacement processes seem to be environmentally unfriendly and complex. Herein, we reported a green and efficient method for the preparation of a lignocellulosic xerogel. The xerogel was fabricated by alkali freezing of unbleached eucalyptus fibers followed by water washing and ambient drying. The alkali freezing promoted fiber swelling and enhanced the hydrogen bonds among the fibers, resulting in the gelation of lignocellulosic fibers. In particular, the residual lignin in the fibers reduced the capillary force during the drying process. The resulting lignocellulosic xerogel achieved a low shrinkage rate (27.50%), low density (0.039 g cm^{-3}), high porosity (97.57%), and excellent mechanical strength (782.23 kPa) as well as environmental stability, and low thermal conductivity (44.76 mW m^{-1} K^{-1}). Similarly structured xerogels could be generated using recycled NaOH solution. This technique was suitable for production using various kinds of plant fibers, which shows its great scalable production prospects.

Introduction

Aerogels are a kind of porous material with a three-dimensional network structure, known for their exceptional properties such as low density, high porosity, and low thermal conductivity.[1–4] These characteristics make aerogels highly suitable for various applications, particularly as thermal insulation materials to reduce the energy consumption in buildings.[5–7] However, their extensive application has been severely restricted by complicated and low efficiency preparation processes.

Generally, aerogels are prepared in two steps, including gel formation and gel drying.[4,8] Currently, most aerogels are dried by freeze-drying or supercritical drying of their hydrogels.[9] Unfortunately, these methods require extreme conditions and expensive equipment, resulting in high cost and low drying efficiency.[10,11] As a result, the research on aerogels has primarily remained in the laboratory stage.

To solve the above-mentioned challenge, the preparation of aerogels using ambient drying technology (named as xerogels) has gained great attention in recent years.[12–14] Considering environmental sustainability, cellulose-based aerogels/xerogels have attracted great attention.[5,15] However, since strong capillary forces exist during the ambient drying due to the intrinsic hydrophilicity of cellulose fibers, strategies have been applied to avoid the collapse of the cellulose-based xerogels. The common method is to replace water with low-surface-tension organic solvents before gel drying to mitigate the influence of capillary forces.[10,12] Additionally, chemical cross-linking has been used to enhance the pore walls to prevent the structural collapse of the xerogel.[16] However, the addition of chemical cross-linkers and prolonged organic solvent replacement processes seem to be inefficient, and also cause extensive consumption of chemicals and environmental pollution. Accordingly, an efficient and large-scale production method to design lignocellulosic xerogels with excellent properties is highly desirable to broaden their practical applications.

Herein, unbleached eucalyptus fibers were frozen in sodium hydroxide solution followed by washing and drying in the atmospheric environment. During the freezing process, the ice crystals acted as a bursting agent, facilitating the penetration of sodium hydroxide into the eucalyptus fibers. This

---

[a] *Guangxi Key Laboratory of Clean Pulp & Papermaking and Pollution Control, College of Light Industry and Food Engineering, Guangxi University, Nanning 530004, China. E-mail: weili@gxu.edu.cn*
[b] *Guangxi Key Laboratory of Natural Polymer Chemistry and Physics, College of Chemistry and Materials Science, Nanning Normal University, Nanning 530001, China*

† Electronic supplementary information (ESI) available. See DOI: **https://doi.org/10.1039/d4gc00825a**

‡ These authors contributed equally to this work.

led to the fiber swelling to achieve gel formation by increased physical entanglement and hydrogen bonds between the fibers. In particular, the residual lignin in the fibers not only increased the contact angle of the fiber/water interface due to its hydrophobicity, but it also increased the pore size of the resulting xerogel. All these effects led to the reduction of capillary forces during gel drying, thereby minimizing the shrinkage of the resulting xerogel. The developed lignocellulosic xerogel exhibited low density, high porosity and low thermal conductivity.

Results and discussion

Preparation process of the lignocellulosic xerogel

The lignocellulosic xerogel was prepared by mechanical milling of unbleached eucalyptus fibers, alkali freezing and ambient drying (Fig. 1a). Mechanical milling of unbleached eucalyptus fibers resulted in fibers with nanoscale dimensions and an increased amount of exposed hydroxyl groups. This would facilitate the formation of hydrogen bonds and physical entanglement among the lignocellulosic nanofibers. The nanofibers were then frozen with NaOH at −20 °C. The partial removal of hemicellulose and lignin in the fibers during the process boosted the amount of cellulose moieties as well as hydroxyl groups. In detail, the ionized OH^- and Na^+ ions in the NaOH solution formed specific sized $[OH(H_2O)_n]^-$ and $[Na(H_2O)_m]^+$ ions with H_2O molecules, respectively, which then penetrated into the fiber interior due to the growth and bursting of ice crystals.[17] This resulted in fiber swelling and the formation of interconnected network structures through enhanced physical entanglement and new hydrogen bonding between the lignocellulosic nanofibers. In contrast, since the $[OH(H_2O)_n]^-$ and $[Na(H_2O)_m]^+$ ions were unstable and struggled to form and maintain the ion structure without freezing, the lignocellulose fibers in NaOH solution could not achieve gel formation at room temperature (Fig. 1b). Additionally, the hydrophobicity of lignin in the eucalyptus fibers reduced the capillary forces during ambient drying, ensuring the integrity of the xerogel structure. In this case, the resulting lignocellulosic xerogel exhibited an ultralight property, shapeability, and excellent mechanical strength (Fig. 1c–e).

Gelation mechanism of the lignocellulosic hydrogel

To explore the formation mechanism of the lignocellulosic xerogel, the chemical structure of cellulose fibers after different treatment periods with cold alkali was analyzed. It's worth noting that only by extending the treatment time to 5 h with an alkali content of 12.5 wt% was the fiber suspension

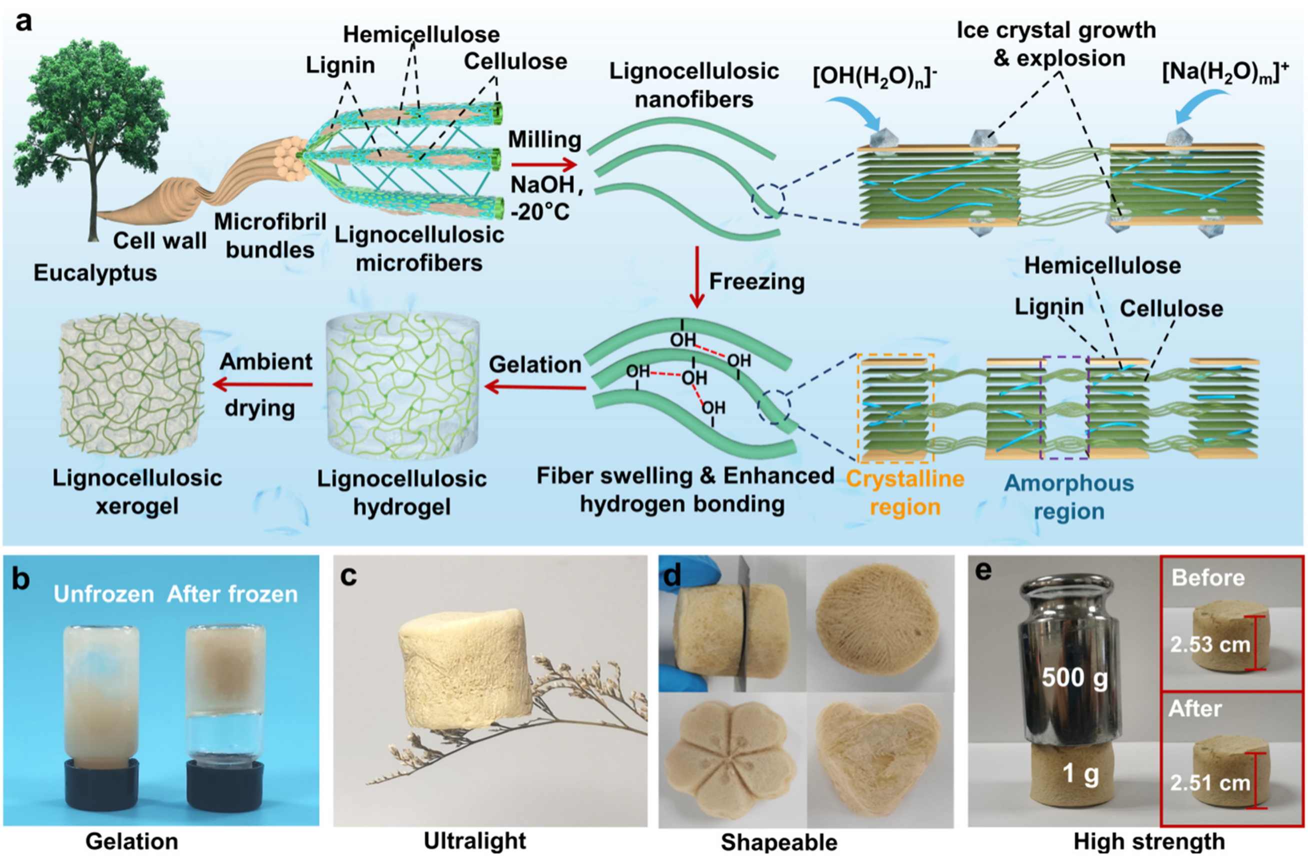

Fig. 1 Preparation process and properties of lignocellulosic xerogels. (a and b) Schematic illustration of the fabrication process of lignocelluosic xerogels (a) and a photo of lignocelluosic hydrogels (b). (c–e) Photos of different properties of lignocellulosic xerogels.

successfully frozen and lignocellulosic hydrogel formed after thawing (Fig. S1†).

The FTIR spectra of pristine cellulose fibers and fibers after different NaOH freezing treatment time periods (3 h and 5 h) are shown in Fig. 2a. As for the pristine fibers, the characteristic peaks at 3309 cm^{-1} and 2892 cm^{-1} were attributed to the stretching vibration of hydroxyl and methylene groups, respectively.[18] The absorbance at 1432 cm^{-1} was assigned to the C–H bending vibration of cellulose and lignin, as well as the aromatic skeletal vibrations of lignin.[18] The bands at 1372 cm^{-1} and 880 cm^{-1} belonged to the C–H deformation vibration and β-glucosidic linkages between the sugar units in the cellulose and hemicellulose, respectively. The peak at 1315 cm^{-1} resulted from the ring breathing with C–O stretching in lignin. The absorbance at 1245 cm^{-1} was ascribed to the CO–OR stretching vibration of hemicellulose and the Ar–O stretching vibration of lignin.[19,20] These results indicated that the pristine fibers exhibited the chemical structure of cellulose, hemicellulose and lignin.

The peak intensity of the characteristic absorption peaks seemed to have no significant changes after 3 h freezing treatment. This phenomenon could be explained by the slow formation of ice crystals in the early stage of freezing and the relatively slow NaOH penetration, which caused limited interaction with the fibers.[21] After freezing for 5 h, the fibers exhibited obvious peak enhancement at 1432 cm^{-1} and 1372 cm^{-1}. Additionally, the C–R (R═C or H) structure in the fibers decreased, and the O–C–O structure significantly increased (Fig. 2b). The growth and bursting of ice crystals made it easier for NaOH to enter the interior of the fibers to destroy the connection between cellulose, hemicellulose and lignin to remove some hemicellulose and lignin (Fig. 2c). To be more precise, the chemical components of the fibers before and after treatment were analyzed by a two-step acid digestion method.[22] Fig. S2a† shows that after 5 h of treatment, the cellulose content increased from 64.60% to 71.05%, while the hemicellulose and lignin contents decreased from 13.77% to 9.05% and 13.16% to 11.33%, respectively. The partial removal of hemicellulose and lignin from the fibers would lead to a higher proportion of cellulose components to form a gel.[23] Further increasing the NaOH content caused further increment of cellulose content as well as decrease of hemicellulose and lignin content (Fig. S2b†). This would make the xerogel have a denser structure, which will be discussed later.

Apart from the chemical structure of the fibers, the fiber swelling performance is of great importance to know due to its

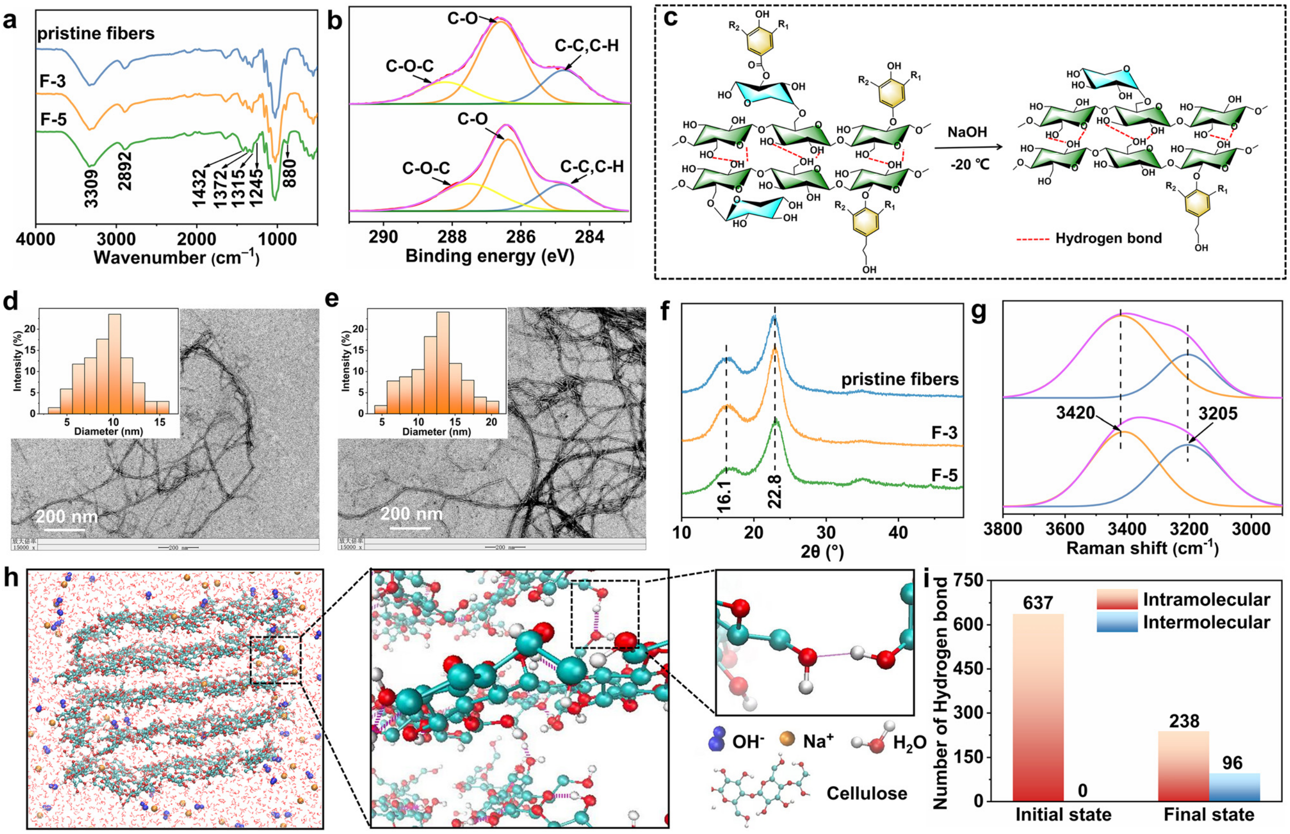

Fig. 2 (a) FTIR spectra of the pristine fibers and fibers treated with different NaOH freezing time periods. (b) High-resolution C 1s XPS spectra of the pristine fibers (top) and $X_{12.5}$ (bottom). (c) Reaction of the fibers in cold alkali. (d and e) TEM images and size distributions of the pristine fibers and the fibers frozen in NaOH for 4 h. (f) XRD spectra of the pristine fibers and fibers treated with different NaOH freezing time periods. (g) Raman spectra of the pristine fiber suspension (top) and lignocellulosic hydrogel (bottom). (h) Molecular dynamics simulations. (i) Number of hydrogen bonds simulated by MDS.

positive role in the buildup of hydrogen bonding among fibers as well as physical entanglement for gel formation. Fig. 2d–e are the TEM images with inserted size distributions of the pristine fibers and fibers frozen in NaOH for 4 h, respectively. It can be seen that the diameter of the pristine and treated fibers ranged from 3 nm to 15 nm and 4 nm to 21 nm, respectively. In order to understand the fiber swelling properties, the crystal structure of fibers treated with NaOH for different time periods was analyzed by XRD. As shown in Fig. 2f, all samples displayed obvious crystallization peaks at 16.1° (110) and 22.8° (002), demonstrating a typical cellulose I structure.[24] With the increase of freezing time, the peak intensity at 22.8° and crystallinity of fibers decreased after the initial increase (Table S1†). The reason for this change could be that the NaOH treatment initially removed the amorphous hemicellulose and lignin, leading to an increased proportion of the cellulose crystalline region. Further increasing the freezing time to 5 h, the ice crystals exploded and extruded, which allowed the NaOH solution to penetrate and disrupt the internal cellulose crystalline structure, leading to fiber swelling.[25] Additionally, since the residual lignin in the cellulose fibers restricted the free movement between fibers, the cellulose I structure partially converted into the cellulose II structure.[26–28] This would be beneficial to the mechanical strength of the resulting xerogel.[29]

Based on the above discussion, the chemical and crystal structures of lignocellulosic fibers displayed obvious changes after NaOH freezing. In the following, the formation mechanism of the lignocellulosic hydrogel is explored. Since the change in the molecular structure of the cellulose fibers will affect their surface charge as well as the fiber aggregation form, the zeta potential of the NaOH/fiber suspensions was analyzed. As seen in Fig. S3,† their zeta potential increased from −23.87 mV to −18.10 mV after freezing for 0 h to 4 h, indicating that the fiber aggregation level gradually increased with the increase of freezing time. This phenomenon could be attributed to the following two factors: (1) the fibers swelled after cold NaOH treatment, which made the fibers become aggregated and entangled; (2) since the polarity of the cellulose II structure was opposite to that of the cellulose I structure, part of the cellulose I structure converting to the cellulose II structure would promote adjacent fibers to bind with each other to form irregular aggregations.[24,30] The fiber aggregation would be beneficial to the gel formation.[31] Furthermore, the hydrogen bonds among cellulose fibers in the pristine fiber suspension and the hydrogel were investigated by Raman spectroscopy. As shown in Fig. 2g, the peaks at 3205 cm^{-1} and 3420 cm^{-1} were attributed to the strongly hydrogen-bonded O–H stretching within the regular tetrahedral coordination and weakly hydrogen-bonded O–H stretching within the incomplete tetrahedral structure, respectively.[32] Thus, the relative intensity of I_{3205}/I_{3420} can be used to calculate the ratio between the strong hydrogen bonds and the weak hydrogen bonds in the system. The higher I_{3205}/I_{3420} ratio in the lignocellulosic hydrogel compared with that in the pristine fiber suspension (Fig. S4†) indicated that the fibers formed more strong hydrogen bonds after NaOH freezing, which would also play a key role in the gel formation.

To further prove the above results, molecular dynamics (MD) simulation was used to simulate the change of the fibers after alkali freezing. Fig. S5† and Fig. 2h show the initial and final structures of cellulose molecules in the NaOH aqueous solution. In the initial stage, the internal structure of cellulose had strong hydrogen bonds, which represented the crystalline region of cellulose fibers. In order to simplify the calculation, the number of hydrogen bonds between cellulose fibers at this stage was set to be 0. After 20 ns of reaction, the number of intramolecular hydrogen bonds in the cellulose fibers decreased from 637 to 238, while the intermolecular hydrogen bonds increased from 0 to 96 (Fig. 2i). This was consistent with the structure changes of the fibers as mentioned above, where the fibers swelled and the bonding between the fibers enhanced. Accordingly, the gelation mechanism of the lignocellulose xerogel could be concluded to be as follows: after NaOH freezing treatment, some of the hemicellulose and lignin in the fibers was removed, and NaOH penetrated into the amorphous and crystalline regions of the cellulose molecules, resulting in the fiber swelling and enhanced fiber aggregation as well as entanglement to increase the hydrogen bonding among fibers to form lignocellulosic hydrogels.

Drying mechanism of the lignocellulosic xerogel

The generated lignocellulosic hydrogel was further dried under ambient conditions to produce the corresponding xerogel. Normally, due to the abundant hydroxyl groups in the cellulose fibers, strong capillary forces may exist during gel drying, leading to the severe shrinkage or even collapse of the xerogel.[9] However, as seen from Fig. 3a, our proposed lignocellulosic xerogel kept good structural integrity with slight shrinkage. With the progressive increase in the NaOH content from 12.5 wt% to 75 wt%, the volume shrinkage of the lignocellulosic xerogel increased from 27.50% to 47.33%, while the density increased from 39.19 ± 1.05 mg cm^{-3} to 71.54 ± 1.15 mg cm^{-3}, and the porosity decreased from 97.57% to 95.73% (Table S2†). In order to explore the shrinkage difference of lignocellulosic xerogels, their morphology was investigated by SEM. As shown in Fig. 3b, the interior of $X_{12.5}$ exhibited an internal lamellar structure, which might enhance the strength of the pore walls to withstand the capillary forces during drying, while more intertwined lignocellulosic fibers appeared in the xerogels with the increase in the NaOH concentration, resulting in smaller pore sizes and denser structures (Fig. 3c–e). These phenomena could be attributed to the change in the crystal structure of the fibers after cold alkali treatment. At low NaOH concentrations, there was a large quantity of the cellulose I structure. As a result, lamellar structures and xerogels with large pore sizes were formed due to the entanglement and aggregation of the cellulose I fibers. In contrast, exposure to higher NaOH concentrations increased the proportion of the cellulose II structure, leading to rapid entanglement of the fibers.[24] This caused significant shrinkage and aggregation of adjacent fibers, ultimately resulting in more compact xerogel structures with smaller pore

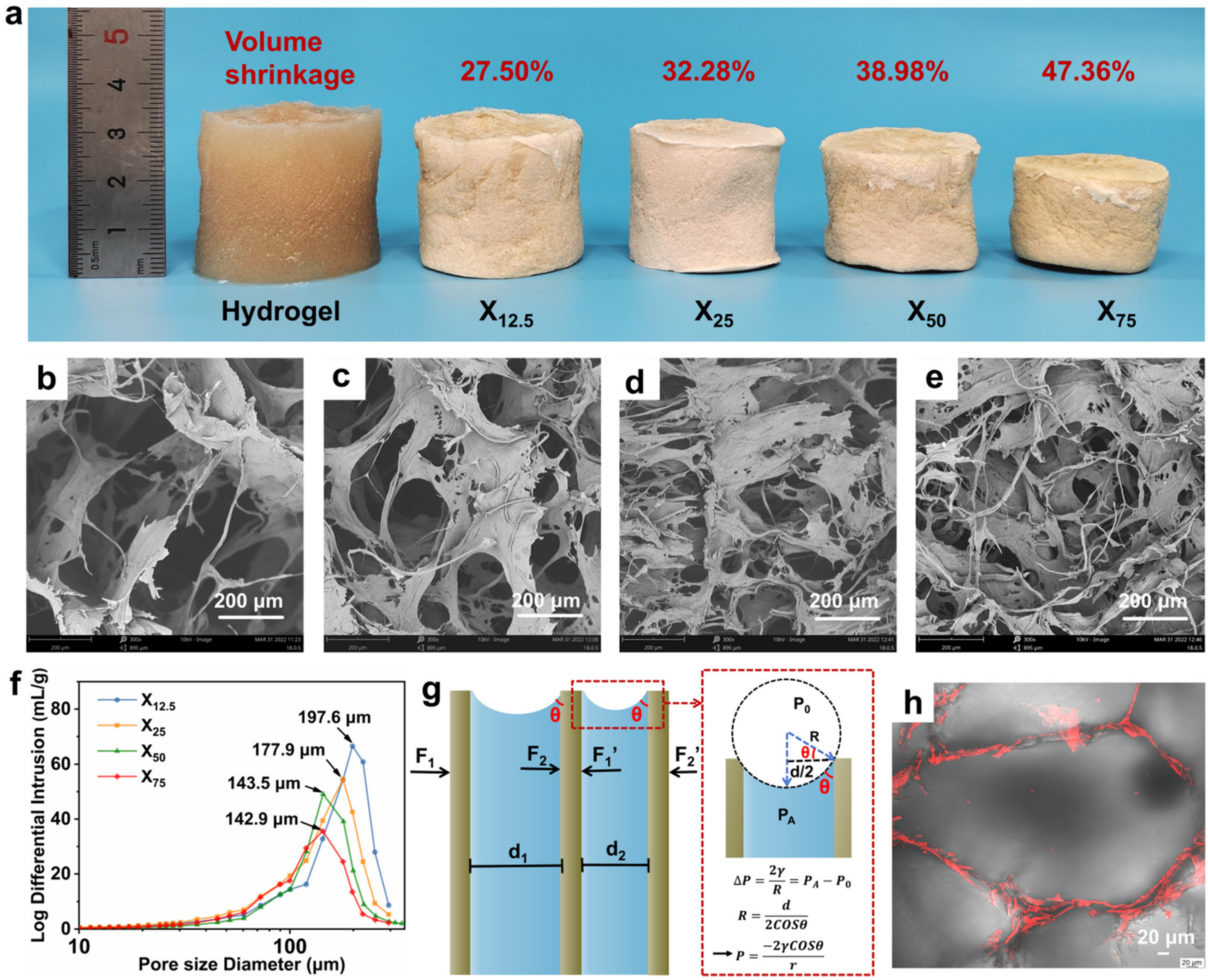

Fig. 3 (a) Pictures of lignocellulosic hydrogel and $X_{12.5-75}$. (b–e) SEM images and (f) pore-size distributions of $X_{12.5-75}$. (g) Stress analysis of the pore wall during hydrogel drying. (h) CLSM image of $X_{12.5}$.

sizes.[33] To be more precise, the pore size of lignocellulosic xerogels decreased from 197.6 µm to 142.9 µm when the NaOH content increased from 12.5 wt% to 75 wt% (Fig. 3f). Additionally, the lignocellulosic xerogels showed an obvious first-order pore size distribution, indicating the uniformity of the obtained xerogels.[34]

To further understand the shrinkage, the capillary forces in the hydrogel during ambient drying were analyzed. As illustrated in Fig. 3g, F_1, F'_1, F_2, and F'_2 are the capillary pressures experienced by the pore walls of the xerogel with different pore sizes in the horizontal direction during the drying process. According to Fig. 3g, the Young–Laplace equation (eqn (1))[35,36] can be derived.

$$P = \frac{-2\gamma\cos\theta}{r} \tag{1}$$

where P is the capillary force, γ is the surface tension, θ is the contact angle, and r is the radius of the pore.

In this case, increasing the pore radius or/and contact angle of the solid–liquid interface of the hydrogel can reduce the capillary force, leading to a low shrinkage of the generated xerogel. It was found that the hydrophobic lignin moieties may hinder the molecular interaction among fibers.[37] This would affect the pore structure of the xerogels and the wetting state of the pore wall with water to further influence the shrinkage of the hydrogel during drying. Thus, lignocellulosic xerogels with different lignin contents were prepared (Fig. S6†). As the lignin content of the fibers decreased (Table S3†), the shrinkage rate of the xerogels increased from 27.50 ± 0.38% to 36.71 ± 1.23%, while the density increased from 39.19 ± 1.05 mg cm^{-3} to 57.80 ± 0.28 mg cm^{-3}, and the porosity decreased from 97.57% to 96.55% (Table S2†). This could be attributed to the lignin not only hindering the formation of hydrogen bonds between cellulose and hemicellulose, but also limiting the swelling capacity of the hydrogel, thus increasing the pore size of the fiber network (Fig. S7†). Furthermore, as shown in the confocal laser scanning microscopy (CLSM) image (Fig. 3h), lignin was uniformly distributed around the pore of the xerogel. Since lignin is hydrophobic, it can reduce the contact angle between the pore wall and the water, which decreased the capillary forces in the system to reduce the volume shrinkage of the xerogel.

Besides the impact of fiber composition, the effect of fiber size on the volume shrinkage of the lignocellulosic xerogel was investigated with the pristine fibers milled for different time periods. As shown in Fig. S8,† compared with $X_{12.5}$ (milled for 120 min), the samples made of the pristine fibers and that milled for 200 min severely shrunk. This result can be attributed to there being fewer hydroxyl groups on the pristine fibers without milling, resulting in the difficulty in the formation of abundant fiber network structures. If the pristine fibers were vigorously milled, the generated nanofibers would form a gel with small pore size, leading to the strong capillary force during drying. Additionally, the shrinkage rate of the lignocellulosic xerogels decreased from 27.50 ± 0.38% to 24.68 ± 0.68% upon adjusting the slurry consistency from 2 wt% to 3 wt%, while the density increased from 39.19 ± 1.05 mg cm^{-3} to 52.43 ± 1.00 mg cm^{-3}, and the porosity decreased from 97.57% to 96.87% (Table S2†). These changes can be ascribed to the increased slurry concentration causing more fiber entanglement in a unit volume, thus enhancing the mechanical properties of the pore wall to resist the effect of the capillary forces. Since the drying speed would also affect the shrinkage rate of the xerogel,[38] the effect of drying temperature on the shrinkage rate of the lignocellulosic xerogel has been investigated. As shown in Table S2,† the shrinkage rate of the xerogels increased from 27.50% to 36.98% when the drying temperature rose from 40 °C to 100 °C. This could be due to the increased evaporation speed caused by the increment of temperature leading to the enhancement of the molecular interaction between water molecules, resulting in strong surface tension and capillary forces.[39] Accordingly, the optimal comprehensive properties of the lignocellulosic xerogels were achieved when the NaOH content was 12.5%, the lignin content of the fibers was 13.16%, the slurry concentration was 2 wt%, and the drying temperature was 40 °C. Under these conditions, the shrinkage rate, density and porosity of the lignocellulosic xerogel were 27.50%, 39.19 mg cm^{-3}, and 97.57%, respectively, which are better than those of most reported cellulose xerogels (Table S4†).[10–12,16,40,41]

Mechanical properties and applications of lignocellulosic xerogels

The mechanical properties of xerogels are crucial for their practical applications. As shown in Fig. S9,† the compressive stress at 40% strain of lignocellulosic xerogels prepared with different NaOH contents were 110.59 ± 0.31 kPa, 71.18 ± 0.25 kPa, 85.64 ± 0.10 kPa and 127.77 ± 0.33 kPa, respectively. The decrease in the compressive stress of the xerogels with the increased NaOH dosages could be due to the gradual removal of hemicellulose and lignin. X_{75} demonstrated the highest mechanical strength due to its smallest pore size, densest network structure, and highest density. Furthermore, the compressive stress of our lignocellulosic xerogel increased with the increment of strain. This was due to the densification of $X_{12.5}$ with the increasing strain.[42,43] At 80% strain, the compressive stress of $X_{12.5}$ was 782.23 ± 0.58 kPa (Fig. 4a), which was higher than those of previously published cellulose aerogels (Table S5†).[9,20,44–47] Moreover, $X_{12.5}$ displayed good height even when compressed by a bicycle (Fig. 4c). In particular, $X_{12.5}$ maintained good mechanical strength even after exposure to extreme conditions such as freezing in liquid nitrogen at −196 °C and heating on a 200 °C hotplate (Fig. 4b). The low temperature of liquid nitrogen may affect the structure of $X_{12.5}$, leading to a slight decrease in mechanical strength. In contrast, under elevated temperature, lignin underwent a pyrolysis reaction and formed new cross-linking structures, thereby enhancing the mechanical strength of $X_{12.5}$.[48] What's more, even after being placed in a constant temperature and humidity environment (25 °C, 57% RH) for 20 days, the shrinkage rate of $X_{12.5}$ remained constant (Fig. 4d). This could be due to the presence of hydrophobic lignin in the fibers. Additionally, $X_{12.5}$ also kept a stable structure in water for 24 h (Fig. S10†), indicating its application prospects in fields such as water pollution treatment, oil–water separation, and seawater evaporation.[49–51] All these results indicated the excellent stability of our proposed lignocellulosic xerogels under extreme conditions.

Since the fabricated lignocellulosic xerogels displayed low density, high porosity and excellent environmental stability, they could be used for energy-saving buildings. In the following, the thermal insulation properties of the xerogels were investigated. As seen in Fig. 4e, the thermal conductivities of $X_{12.5}$, X_{25}, X_{50} and X_{75} were 44.76 mW m^{-1} K^{-1}, 47.43 mW m^{-1} K^{-1}, 53.12 mW m^{-1} K^{-1} and 56.33 mW m^{-1} K^{-1}, respectively. In general, the total heat transfer (λ_t) of aerogels consists of four parts: thermal convection (λ_c), solid phase conduction (λ_s), conduction through the gaseous phase (λ_g), and radiative heat transfer through pores (λ_r).[52] The lowest density and the three-dimensional network structure (the pore size is <1 mm) of $X_{12.5}$ could efficiently reduce λ_s and λ_c, respectively, leading to the lowest thermal conductivity. The thermal conductivity of $X_{12.5}$ was lower than those commercial thermal insulating materials and cellulose composite aerogels (Fig. 4f),[53–59] indicating its good application prospects.

To further investigate the thermal insulation properties of the lignocellulosic xerogel, $X_{12.5}$ was placed on a heating platform at 100 °C and copper plates at liquid nitrogen temperature for 30 min (Fig. 4g). Infrared thermal images showed that the temperature of $X_{12.5}$ increased from 39.9 °C to 49.0 °C and decreased from 22.3 °C to 17.6 °C under the above conditions, demonstrating its excellent thermal insulation performance. Interestingly, when the xerogels were placed on a hand and a mobile phone, the covered areas turned blue, blending with the ambient color, and the covered areas almost "disappeared" in the infrared thermal images (Fig. 4h). This indicated the potential application of our lignocellulosic xerogels as thermal stealth materials. Additionally, as shown in Fig. 4i, a quartz

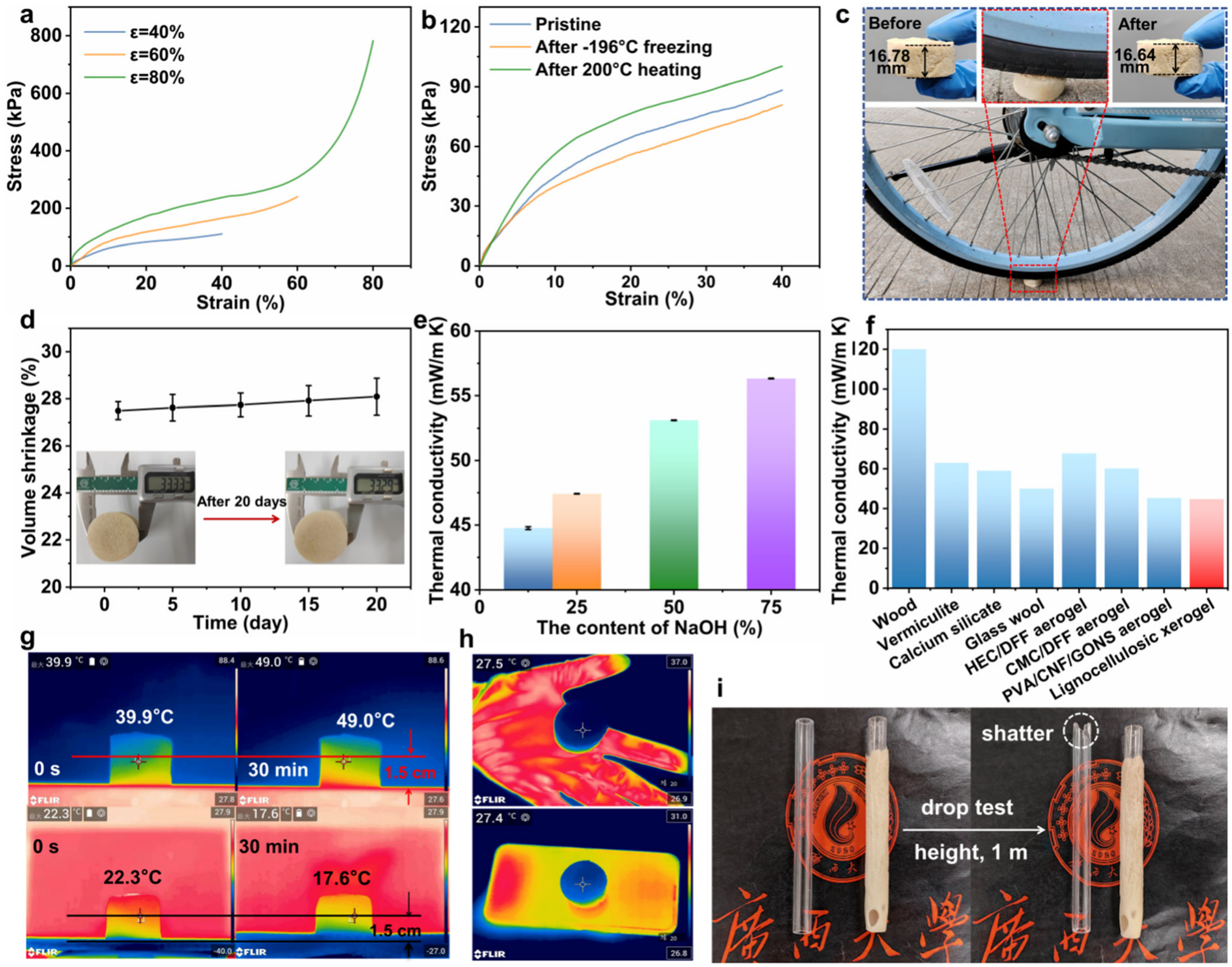

Fig. 4 (a) Stress–strain curves of $X_{12.5}$ at 40, 60 and 80% strain. (b) Stress–strain curves of $X_{12.5}$ after liquid nitrogen and 200 °C treatment. (c) Picture of $X_{12.5}$ compressed by a bicycle. (d) Volume change of $X_{12.5}$ after being placed in a constant temperature and humidity environment for 20 days. (e) Thermal conductivity of $X_{12.5-75}$. (f) Comparison of thermal conductivity and density between $X_{12.5}$ and other thermally insulating materials. (g) Infrared thermal images of $X_{12.5}$ on a heating platform (100 °C, top) and liquid nitrogen-cooled copper plate (bottom). (h) Infrared thermal images of $X_{12.5}$ placed on a hand (top) and a mobile phone (bottom). (i) Comparison between a quartz glass tube and a quartz glass tube wrapped with $X_{12.5}$ before and after a drop test.

glass tube and a quartz glass tube wrapped with $X_{12.5}$ were simultaneously dropped from a height of 1 m onto a ceramic tile floor. The quartz glass tube shattered, while the quartz glass tube wrapped with $X_{12.5}$ remained intact after the test. This suggested the potential of xerogels for shock absorption and protection of fragile and brittle materials.

Large-scale preparation of lignocellulosic xerogels and solvent recyclability

Considering the feasibility of the preparation method, a lignocellulosic xerogel with a size of ∅160 mm × 60 mm was successfully prepared (Fig. 5a). Additionally, agricultural and forestry waste materials (such as bagasse, corn stalks and straw) could be also used as raw materials to prepare xerogels with a complete structure (Fig. 5b). Due to the difference of lignin contents in the raw materials, their shrinkage rates were 31.99%, 32.58% and 32.43%, respectively. Even though the lignocellulosic aerogel prepared by freeze-drying displayed better density (27.91 mg cm^{-3}) and porosity (98.34%), the freeze-drying process took more time (Table S6†). Thanks to the simplicity of the preparation method and the wide sources of raw materials, large-scale production of xerogels would be feasible (Fig. 5c).

As for large-scale preparation, the recyclability of chemicals needs to be evaluated. According to our proposed NaOH circulation reaction system (Fig. 5e), the recycling rate of the filtrate obtained after washing the hydrogel was as high as 69.30%. The recycled NaOH solution could be used to prepare lignocellulosic xerogel ($R_{12.5}$), which could reduce the use of NaOH by 41.6% in comparison with the original preparation process. In particular, the volume shrinkage ratio, density, porosity and compressive stress of the prepared $R_{12.5}$ were similar to those

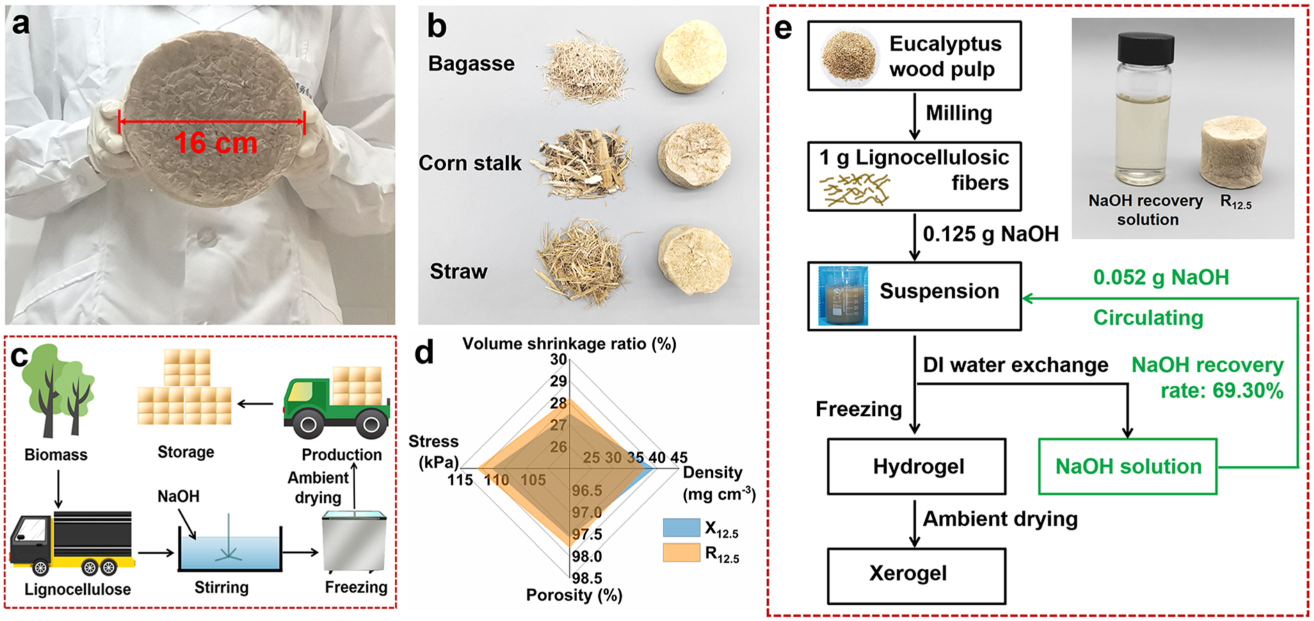

Fig. 5 (a) Picture of a large-sized xerogel (∅160 mm × 60 mm). (b) Pictures of xerogels prepared from bagasse, corn stalk and straw. (c) Schematic diagram of the mass production and application of xerogels. (d) Radar diagram of the comprehensive properties of a xerogel ($R_{12.5}$) prepared from recycled NaOH solution and $X_{12.5}$. (e) Schematic diagram of the recycling procedure of NaOH solution.

of the original $X_{12.5}$ (Fig. 5d). All these results indicated the good recyclability of our preparation method for lignocellulosic xerogels.

Conclusion

Lignocellulosic xerogels were fabricated by mechanical milling of unbleached eucalyptus fibers, alkali freezing and ambient drying. During the freezing process, fiber swelling played a key role in the gel formation by increasing physical entanglement and hydrogen bonding between the fibers. Additionally, the residual lignin in the fibers could increase the pore size of the xerogel and the contact angle of the fiber–water interface, which alleviated the capillary forces during gel drying, thereby minimizing the shrinkage of the resulting xerogels (27.50%). The lignocellulosic xerogel exhibited low density, high porosity, excellent mechanical strength and environmental durability. The method in this study could be applied for scalable preparation of various bio-based xerogels with solvent recycling. Our proposed fabrication strategy could be an important guideline for the development of bio-based aerogels to promote their practical applications.

Author contributions

Qiaoling Huang: methodology, data curation, investigation, formal analysis, and writing – original draft. Zerong Li: data curation, investigation, formal analysis, and writing – review & editing. Jialong Hu: software and resources. Wei Wang: funding acquisition and resources. Wei Li: conceptualization, funding acquisition, project administration, supervision, writing – review & editing.

Conflicts of interest

There are no conflicts to declare.

Acknowledgements

This work was supported by the Natural Science Foundation of Guangxi (2018GXNSFBA138027), the Scientific Research Foundation of Guangxi University (XGZ170232), the Foundation of Guangxi Key Laboratory of Clean Pulp & Papermaking and Pollution Control (No. 2023GXZZKF75) and the Training Program for Thousand Young and Middle-aged Backbone Teachers in Colleges of Guangxi.

References

1 X. Q. Li, X. M. Lu, J. M. Yang, Z. Y. Ju, Y. Kang, J. L. Xu and S. J. Zhang, *Green Chem.*, 2019, **21**, 2699–2708.
2 Y. S. Fei, Y. J. Tan, Y. Y. Deng, P. Z. Xia, J. R. Cheng, C. C. Wang, J. J. Zhang, C. X. Niu, Q. Fu and L. B. Lu, *Green Chem.*, 2022, **24**, 7074–7081.
3 Y. Kong, X. D. Shen, S. Cui and M. H. Fan, *Green Chem.*, 2015, **17**, 3436–3445.
4 V. Rahmanian, T. Pirzada, S. Y. Wang and S. A. Khan, *Adv. Mater.*, 2021, **33**, 26.

5 J. W. Song, C. J. Chen, Z. Yang, Y. D. Kuang, T. Li, Y. J. Li, H. Huang, I. Kierzewski, B. Y. Liu, S. M. He, T. T. Gao, S. U. Yuruker, A. Gong, B. Yang and L. B. Hu, *ACS Nano*, 2018, **12**, 140–147.

6 X. K. Zhang, N. Li, Z. M. Hu, J. R. Yu, Y. Wang and J. Zhu, *Chem. Eng. J.*, 2020, **388**, 7.

7 Y. H. Hu, G. Yang, J. T. Zhou, H. Y. Li, L. Shi, X. L. Xu, B. W. Cheng and X. P. Zhuang, *ACS Nano*, 2022, **16**, 5984–5993.

8 R. Du, J. O. Joswig, R. Huebner, L. Zhou, W. Wei, Y. Hu and A. Eychmueller, *Angew. Chem., Int. Ed.*, 2020, **59**, 8293–8300.

9 Y. Y. Li, V. A. Tanna, Y. L. Zhou, H. H. Winter, J. J. Watkins and K. R. Carter, *ACS Sustainable Chem. Eng.*, 2017, **5**, 6387–6391.

10 M. S. Toivonen, A. Kaskela, O. J. Rojas, E. I. Kauppinen and O. Ikkala, *Adv. Funct. Mater.*, 2015, **25**, 6618–6626.

11 G. Pour, C. Beauger, A. Rigacci and T. Budtova, *J. Mater. Sci.*, 2015, **50**, 4526–4535.

12 S. Yamasaki, W. Sakuma, H. Yasui, K. Daicho, T. Saito, S. Fujisawa, A. Isogai and K. Kanamori, *Front. Chem.*, 2019, **7**, 8.

13 Y. Luo, Z. Li, W. Zhang, H. Yan, Y. F. Wang, M. Li and Q. Liu, *J. Non-Cryst. Solids*, 2019, **503**, 214–223.

14 R. L. Wang, C. J. Chen, Z. Q. Pang, X. Z. Wang, Y. B. Zhou, Q. Dong, M. Guo, J. L. Gao, U. Ray, Q. Q. Xia, Z. W. Lin, S. M. He, B. Foster, T. Li and L. B. Hu, *Nano Lett.*, 2022, **22**, 3931–3938.

15 F. Jiang, H. Liu, Y. Li, Y. D. Kuang, X. Xu, C. J. Chen, H. Huang, C. Jia, X. P. Zhao, E. Hitz, Y. B. Zhou, R. G. Yang, L. F. Cui and L. B. Hu, *ACS Appl. Mater. Interfaces*, 2018, **10**, 1104–1112.

16 Y. Z. Li, N. Grishkewich, L. L. Liu, C. Wang, K. C. Tam, S. Q. Liu, Z. P. Mao and X. F. Sui, *Chem. Eng. J.*, 2019, **366**, 531–538.

17 J. Cai, L. Zhang, S. L. Liu, Y. T. Liu, X. J. Xu, X. M. Chen, B. Chu, X. L. Guo, J. Xu, H. Cheng, C. C. Han and S. Kuga, *Macromolecules*, 2008, **41**, 9345–9351.

18 S. Yang, W. T. He, Y. Fu, Y. Zhang, T. Q. Yuan and R. C. Sun, *Ind. Crops Prod.*, 2017, **98**, 38–45.

19 M. J. Chen, X. Q. Zhang, A. P. Zhang, C. F. Liu and R. C. Sun, *Cellulose*, 2016, **23**, 1325–1334.

20 Z. R. Li, Y. P. Zhang, Q. L. Huang, Z. L. Chen, W. Wang and W. Li, *ACS Appl. Mater. Interfaces*, 2023, **15**, 11827–11836.

21 F. Y. Zeng, S. S. Wang, J. R. Liang, L. M. Cao, X. X. Liu, C. R. Qin, C. Liang, C. L. Si, Z. B. Yu and S. Q. Yao, *Bioresour. Technol.*, 2022, **361**, 9.

22 J. Y. Ge, Y. T. Wu, Y. S. Han, C. R. Qin, S. X. Nie, S. J. Liu, S. F. Wang and S. Q. Yao, *Bioresour. Technol.*, 2020, **307**, 9.

23 S. I. Mussatto, G. Dragone, M. Fernandes, A. M. F. Milagres and I. C. Roberto, *Cellulose*, 2008, **15**, 711–721.

24 S. X. Nie, C. Y. Zhang, Q. Zhang, K. Zhang, Y. H. Zhang, P. Tao and S. F. Wang, *Ind. Crops Prod.*, 2018, **124**, 435–441.

25 L. K. Lazzari, V. B. Zampieri, A. J. Zattera and C. Baldasso, *J. Renewable Mater.*, 2019, **7**, 227–234.

26 P. Tao, Y. Zhang, Z. Wu, X. Liao and S. Nie, *Carbohydr. Polym.*, 2019, **214**, 1–7.

27 N. H. Kim, *J. Wood Sci.*, 2005, **51**, 290–294.

28 K. Abe and H. Yano, *Carbohydr. Polym.*, 2011, **85**, 733–737.

29 K. Abe and H. Yano, *Cellulose*, 2012, **19**, 1907–1912.

30 H. Lee, J. Sundaram, L. Zhu, Y. P. Zhao and S. Mani, *Carbohydr. Polym.*, 2018, **181**, 506–513.

31 H. Yano and K. Abe, *Sustain. Humanosphere*, 2012, **2012**, 8.

32 S. Bai, X. H. Li, R. C. Zhang, C. Li, K. Y. Zhu, P. C. Sun, Y. H. Zhao, L. X. Ren and X. Y. Yuan, *Chem. Eng. J.*, 2019, **357**, 667–677.

33 V. Zepic, P. Oven, M. Cop, V. Vek, B. Jankovic and I. Poljansek, *J. Nat. Fibers*, 2022, **19**, 16040–16052.

34 M. L. Zhang, M. M. Li, Q. Y. Xu, W. Jiang, M. H. Hou, L. F. Guo, N. Wang, Y. J. Zhao and L. F. Liu, *Ind. Crops Prod.*, 2022, **179**, 13.

35 B. H. Wang, W. B. Zhang, W. Zhang, A. S. Mujumdar and L. X. Huang, *Drying Technol.*, 2005, **23**, 7–32.

36 H. Maleki, L. Duraes, C. A. García-González, P. del Gaudio, A. Portugal and M. Mahmoudi, *Adv. Colloid Interface Sci.*, 2016, **236**, 1–27.

37 W. Li, Z. R. Li, W. Wang, Z. H. Li, Q. Li, C. R. Qin and F. S. Cao, *Ind. Crops Prod.*, 2021, **172**, 10.

38 C. J. Xie, S. Y. Liu, Q. G. Zhang, H. X. Ma, S. X. Yang, Z. X. Guo, T. Qu and X. L. Tuo, *ACS Nano*, 2021, **15**, 10000–10009.

39 N. Kumar and J. H. Arakeri, *Drying Technol.*, 2020, **38**, 1194–1206.

40 A. Ebrahimi, B. Dahrazma and M. Adelifard, *J. Porous Mater.*, 2020, **27**, 1219–1232.

41 N. Buchtová and T. Budtova, *Cellulose*, 2016, **23**, 2585–2595.

42 S. J. Wang, W. Y. Meng, H. F. Lv, Z. X. Wang and J. W. Pu, *Carbohydr. Polym.*, 2021, **270**, 11.

43 D. G. Jiang, J. Z. Zhang, S. Qin, Z. Y. Wang, K. A. S. Usman, D. Hegh, J. Q. Liu, W. W. Lei and J. M. Razal, *ACS Nano*, 2021, **15**, 5000–5010.

44 H. F. Qin, Y. F. Zhang, J. G. Jiang, L. L. Wang, M. Y. Song, R. Bi, P. H. Zhu and F. Jiang, *Adv. Funct. Mater.*, 2021, **31**, 9.

45 Y. L. Zhu, Z. Y. Yu, J. Y. Zhu, Y. F. Zhang, X. Y. Ren and F. Jiang, *Chem. Eng. J.*, 2022, **445**, 10.

46 S. Jiang, M. L. Zhang, M. M. Li, L. Liu, L. F. Liu and J. Y. Yu, *Cellulose*, 2020, **27**, 6217–6233.

47 Z. H. Zeng, E. Mavrona, D. Sacré, N. Kummer, J. M. Cao, L. A. E. Müller, E. Hack, P. Zolliker and G. Nyström, *ACS Nano*, 2021, **15**, 7451–7462.

48 H. L. Zhu, W. Luo, P. N. Ciesielski, Z. Q. Fang, J. Y. Zhu, G. Henriksson, M. E. Himmel and L. B. Hu, *Chem. Rev.*, 2016, **116**, 9305–9374.

49 X. Y. Zhang, C. Y. Li, L. Dai, C. L. Si, Z. Q. Shen, Z. G. Qiu and J. F. Wang, *J. Environ. Chem. Eng.*, 2023, **11**, 27.

50 S. X. Nie, C. J. Chen and C. J. Zhu, *Front. Chem. Sci. Eng.*, 2023, **17**, 795–797.

51 J. J. Yang, X. S. Han, W. S. Yang, J. P. Hu, C. M. Zhang, K. M. Liuand and S. H. Jiang, *Environ. Res.*, 2023, **236**, 30.

52 Q. Fan, R. X. Ou, X. L. Hao, Q. Y. Deng, Z. Z. Liu, L. C. Sun, C. Q. Zhang, C. G. Guo, X. J. Bai and Q. W. Wang, *ACS Nano*, 2022, **16**, 9062–9076.

53 K. K. Liu, Q. Jiang, S. Tadepallifit, R. Raliya, P. Biswas, R. R. Naik and S. Singamaneni, *ACS Appl. Mater. Interfaces*, 2017, **9**, 7675–7681.

54 M. S. Al-Homoud, *Build. Environ.*, 2005, **40**, 353–366.

55 S. Copiello, *Energy Build.*, 2016, **123**, 59–70.

56 H. R. Kymäläinen and A. M. Sjöberg, *Build. Environ.*, 2008, **43**, 1261–1269.

57 W. H. Sun, Y. C. Fang and L. S. Wu, *J. Porous Mater.*, 2023, **30**, 195–200.

58 W. H. Sun, Y. C. Fang, L. S. Wu and X. H. Liu, *J. Porous Mater.*, 2023, **30**, 989–997.

59 A. Javadi, Q. F. Zheng, F. Payen, A. Javadi, Y. Altin, Z. Y. Cai, R. Sabo and S. Q. Gong, *ACS Appl. Mater. Interfaces*, 2013, **5**, 5969–5975.